

# Average Ionospheric Electric Field Morphologies during Geomagnetic Storm Phases

Maria-Theresia Walach<sup>1,1</sup>, Adrian Grocott<sup>1,1</sup>, and Stephen E. Milan<sup>2,2</sup>

<sup>1</sup>Lancaster University

<sup>2</sup>University of Leicester

November 30, 2022

## Abstract

We utilise Principal Component Analysis to identify and quantify the primary electric potential morphologies during geomagnetic storms. Ordering data from the Super Dual Auroral Radar Network (SuperDARN) by geomagnetic storm phase, we are able to discern changes that occur in association with the development of the storm phases. Along with information on the size of the patterns, the first 6 eigenvectors provide over ~80% of the variability in the morphology, providing us with a robust analysis tool to quantify the main changes in the patterns. Studying the first 6 eigenvectors and their eigenvalues with respect to storm phase shows that the primary changes in the morphologies with respect to storm phase are the convection potential enhancing and the dayside throat rotating from pointing towards the early afternoon sector to being more sunward aligned during the main phase of the storm. We find that the ionospheric electric potential increases through the main phase and then decreases after the end of the main phase is reached. The dayside convection throat points towards the afternoon sector before the main phase and then as the potential increases throughout the main phase, the dayside throat rotates towards magnetic noon. Furthermore, we find that a two cell convection pattern is dominant throughout and that the dusk cell is overall stronger than the dawn cell.

# Average Ionospheric Electric Field Morphologies during Geomagnetic Storm Phases

M.-T. Walach<sup>1</sup>, A. Grocott<sup>1</sup>, S. E. Milan<sup>2</sup>

<sup>1</sup>Lancaster University, Lancaster, LA1 4YW, UK

<sup>2</sup>University of Leicester, Leicester, LE1 7RH, UK

## Key Points:

- Using Principal Component Analysis on SuperDARN data we identify the primary contributing basis convection patterns to ionospheric electric field morphologies during geomagnetic storm times
- The first 6 eigenvectors of the analysis provide over 80% of the total variance, excluding expansions and contractions of the pattern
- The main changes in the electric field that are ordered by storm phase are an enhancement of the convection potential and a motion towards later local times of the dayside convection throat

---

Corresponding author: Maria-Theresia Walach, [m.walach@lancaster.ac.uk](mailto:m.walach@lancaster.ac.uk)

## Abstract

We utilise Principal Component Analysis to identify and quantify the primary electric potential morphologies during geomagnetic storms. Ordering data from the Super Dual Auroral Radar Network (SuperDARN) by geomagnetic storm phase, we are able to discern changes that occur in association with the development of the storm phases. Along with information on the size of the patterns, the first 6 eigenvectors provide over  $\sim 80\%$  of the variability in the morphology, providing us with a robust analysis tool to quantify the main changes in the patterns. Studying the first 6 eigenvectors and their eigenvalues with respect to storm phase shows that the primary changes in the morphologies with respect to storm phase are the convection potential enhancing and the dayside throat rotating from pointing towards the early afternoon sector to being more sunward aligned during the main phase of the storm. We find that the ionospheric electric potential increases through the main phase and then decreases after the end of the main phase is reached. The dayside convection throat points towards the afternoon sector before the main phase and then as the potential increases throughout the main phase, the dayside throat rotates towards magnetic noon. Furthermore, we find that a two cell convection pattern is dominant throughout and that the dusk cell is overall stronger than the dawn cell.

## Plain Language Summary

During geomagnetic storms we see extreme changes to Earth's magnetic field structure. This is mainly due to an enhancement of electrical currents in geospace. This changes the Earth's magnetic environment, due to which we also see changes in the ionosphere, the layer of charged particles making up the top of the atmosphere where the current systems close. A geomagnetic storm has three phases: the initial phase, which is a precursor to the storm, the main phase where the current systems enhance abruptly, and a recovery phase. In this paper we use a technique commonly used for pattern recognition to radar data to work out the changes to the average ionospheric flows. We find that most of the changes happen on the dayside. We suggest this means the average storm dynamics are driven directly by the solar wind.

## 1 Introduction

Geomagnetic storms are understood to be enhancements in the Earth’s ring current (Akasofu & Chapman, 1961; Gonzalez et al., 1994). This westward-flowing current causes large-scale deviations in the Earth’s magnetic field, such that they can be measured on the ground (e.g. Graham, 1724; Chapman & Dyson, 1918; Chapman & Ferraro, 1930; Chapman & Bartels, 1940; Singer, 1957; Daglis et al., 1999). At mid-latitudes, this effect is strongest and registers as a southward deviation in the horizontal north-south magnetometer measurements. These measurements are often combined to give a magnetic index, which can be used to identify storms, such as the Dst index (Sugiura, 1964) or Sym-H index (Iyemori, 1990).

Notable effects of geomagnetic storms not only include changes in the global magnetic field and strengthening of the magnetospheric and ionospheric current systems, but also changes in the ionosphere, such as higher measured densities in the total electron content in the mid-to-low latitudes, which can drift and enhance ionospheric densities at higher latitudes to form storm-enhanced densities (SEDs) and thus also enter the polar cap, forming tongues-of-ionization (TOIs) (e.g. Foster, 1993; Huba et al., 2005; Lin et al., 2005; Mannucci et al., 2008; Thomas et al., 2013; Zou et al., 2013, 2014, and references therein). SEDs in particular have been linked to equatorward expansion of the convection pattern (Zou et al., 2013, 2014) and it is thus important to understand the high-latitude ionospheric electric field as it evolves throughout geomagnetic storms as it will help us understand plasma transport in the ionosphere and magnetosphere.

Whilst ground magnetometer studies can be used to infer the ionospheric electric field (Kamide et al., 1981), direct measurements of plasma convection can also be utilised to build maps of the high-to-mid latitude ionospheric electric fields (e.g. Hairston & Heelis, 1993; Ruohoniemi & Greenwald, 1996). In a previous study, Walach and Grocott (2019) (from here on referred to as WG19) studied ionospheric measurements from the Super Dual Auroral Radar Network (SuperDARN) during the three phases of geomagnetic storms: the initial, main and recovery phase, identified using Sym-H.

WG19 examined the general trends in the SuperDARN data during geomagnetic storms, such as latitudinal expansion of the ionospheric convection maps, data coverage, data availability, cross polar cap potential (i.e. convection strength), in relation to solar wind and geomagnetic conditions. The study also compared statistically the responses



of these measured parameters during geomagnetic storm phases, to periods of disturbed geomagnetic activity, irrespective of storm phase, as well as high solar wind driving when no storms occurred. One of the primary results of this paper was that the storm phases, as well as the ionospheric responses measured by SuperDARN are closely tied to the solar wind driving of the system, which matches previous results (e.g. Loewe & Prölss, 1997; Gillies et al., 2011): During the main phase of a geomagnetic storm, higher solar wind driving due to southward interplanetary magnetic field (negative  $B_Z$ ) enhances the current systems connecting the ionosphere with the magnetosphere. We thus see a higher cross polar cap potential, as well as an enhanced Sym-H index, matching our understanding of how the system works (e.g. Milan et al., 2017). WG19 showed that throughout a geomagnetic storm there is some asymmetry in the two-cell convection pattern measured by SuperDARN, with the dusk cell being much stronger than the dawn cell, as well as changes throughout the storms in the location where the fastest flows are measured in the ionosphere: This is primarily on the dayside, though in the initial and recovery phase the fastest flows are primarily measured in the noon to early morning sectors whereas during the main phase of a storm, this is shifted towards the afternoon sectors. WG19 also found that the return flow boundary (the latitudinal location where antisunward flows neighbour the sunward flows) and the Heppner-Maynard boundary (Heppner & Maynard, 1987) (the boundary where the high-latitude ionospheric convection pattern terminates) move throughout the storm phases, as does the latitudinal distance between them.

Other previous studies using SuperDARN data from geomagnetic storm periods have looked at the number of scatter echoes and line-of-sight velocities in relation to sudden storm commencements (SSC) and sudden commencements (SC) (e.g. Gillies et al., 2012; Kane & Makarevich, 2010), but without a detailed quantitative analysis of ionospheric convection morphologies. A further statistical study by (Gabrielse et al., 2019) compared the mesoscale flows measured by SuperDARN during the main phases and recovery phases, as well as coronal mass ejection (CME) and highspeed stream (HSS) storms. Whilst WG19 did not split the data into the exact same categories, the results broadly agree with these previous studies. Here we only focus on the geomagnetic storm phases to learn about the average ionospheric behaviour. Whilst WG19 answers some basic questions on the morphology and latitudinal extent of ionospheric convection during the phases of a geomagnetic storm, we will examine the morphologies of geomagnetic storms in more

detail here. In this paper, we will study these data further to answer the following question: How do ionospheric convection morphologies change throughout the storm phases?

We answer this question by utilising an objective method for dimensionality reduction (Principal Component Analysis (e.g. Joliffe, 2002)), which will tell us what the primary morphologies in the data are with respect to storm phase.

## 2 Data

There are two primary datasets used in this study: The geomagnetic storm list and the SuperDARN data, which we describe in this section.

### 2.1 Geomagnetic Storms

The geomagnetic storm list is published by WG19 and can be found in their supplementary material. It is formed by applying an automatic identification algorithm to the Sym-H index, which reflects enhancements in the global ring current (Iyemori, 1990). The algorithm identifies the initial, main and recovery phases of geomagnetic storms, similar to Hutchinson et al. (2011), which allows us to draw conclusions about the phenomena associated with the progression of storms. In brief, the initial phase of a geomagnetic storm is classified by a positive excursion in the Sym-H index, associated with an increase in the Ferraro-Chapman currents along the magnetopause, followed by a decrease to below  $-80$  nT during the main phase, where the ring current enhances. The minimum in Sym-H coincides with the end of the main phase, which is followed by a gradual increase to normal values, known as the recovery phase. For further detail, the reader is referred to WG19.

### 2.2 SuperDARN

SuperDARN consists of high-frequency coherent scatter radars built to study ionospheric convection by means of Doppler-shifted, pulse sequences (e.g. Greenwald et al., 1995; Ruohoniemi & Greenwald, 1996; Chisham et al., 2007; Nishitani et al., 2019). Measurements by this large-scale network of radars are used to construct a high-time resolution picture of high-latitude ionospheric convection (Ruohoniemi & Baker, 1998).

With the expansion of the SuperDARN network to mid-latitudes, we are able to study the dynamics of the high-to-mid-latitude ionospheric convection with unprecedented

coverage (Nishitani et al., 2019). One of the findings by WG19 was that the high-latitude convection maps which can be produced with SuperDARN data can expand to  $40^\circ$  of geomagnetic latitude during disturbed times, which was not accounted for in previous versions of the SuperDARN Radar Software Toolkit (RST versions  $< 4.2$ ), which had a cut-off of  $50^\circ$  magnetic latitude. The finding of this expansion matches magnetometer and spacecraft measurements from previous studies (e.g. Wilson et al., 2001; Kikuchi et al., 2008).

The SuperDARN data used here were therefore processed using the Radar Software Toolkit (RST) (SuperDARN Data Analysis Working Group et al., 2018), which is specifically designed to accomodate SuperDARN observations down to  $40^\circ$  of magnetic latitude. Typically, to make SuperDARN convection maps several steps of processing have to be followed: 1) Using RST, an autocorrelation function is fitted to the raw radar data. This produces fitacf files, which store the line-of-sight velocity data. 2) The data is then gridded onto an equal area latitude-longitude grid (see equation 1 from Ruohoniemi & Baker, 1998) and split into two minute cadence records. 3) Data from different radars are combined and the spherical harmonic fitting algorithm is performed which fits an electrostatic potential in terms of spherical harmonic functions to the data (Ruohoniemi & Greenwald, 1996; Ruohoniemi & Baker, 1998). When this fitting is performed, typically a background model, parameterised by solar wind conditions is used, to infill information in the case of data gaps (e.g. Thomas & Shepherd, 2018). Alongside this, a Heppner-Maynard boundary (HMB) (Heppner & Maynard, 1987), the low-latitude boundary of the convection pattern where the flows approach zero, can either be specified or be chosen using the data. This is to constrain the convection pattern when the spherical harmonic fit is applied (Shepherd & Ruohoniemi, 2000). For typical 2-minute convection maps, it is appropriate to use the data to find a threshold of three radar velocity measurements of greater than  $100 \text{ ms}^{-1}$  for the HMB (Imber et al., 2013).

For the purpose of this study, we make 2 minute cadence superposed epoch convection maps, where data from the different storms are combined. This differs slightly to the usual steps outlined above and is explained further in the following section.

We utilise the same storm list and the same gridded SuperDARN data, spanning from 2010-2016, as published in WG19. We have 54 storms with the median storm du-

ration for each storm phase of 19.5 hours for the initial phase, 9.1 hours for the main phase and 55.8 hours for the recovery phase.

### 3 Method

In order to study the characteristic ionospheric convection morphologies of the storms in detail, we make a superposed epoch analysis. Similarly to Hutchinson et al. (2011) and Wharton et al. (2020), we make a superposed epoch analysis of the storms which treats each storm phase independently and scales each phase to the beginning and end, using the median duration. This means that each storm phase duration is scaled to be the same and we can thus compare average characteristics across storms.

We apply our method to the SuperDARN data to make average storm convection maps, which are parameterised by storm phase and median duration: We use the gridded data from the previous study (WG19), and write new convection maps for each storm phase, which are thus time-normalised and comprise the data from all storms. In order to make the convection maps, we write files with all the data and run the map-fitting procedure using RST v4.2 (SuperDARN Data Analysis Working Group et al., 2018) and a 8<sup>th</sup> order spherical harmonic expansion (Ruohoniemi & Greenwald, 1996). This differs slightly to the usual method described earlier: In order to make the storm maps, no statistical background model was used, as the data coverage is very good when combining data from 7 years of geomagnetic storms. As data coverage at lower latitudes can be sparse, especially during the initial phase, the automatic HMB algorithm can select unrealistic boundaries. We avoid this by forcing the HMB to match the lower quartile of the distribution of HMBs from the individual maps per timestep per phase (this is shown in Fig. 8 in WG19 and the second panel from the top in Figure 4 in this paper). To minimize unphysical artefacts dominating the dayside potential, we add padding below the HMB on the dayside by adding artificial datapoints with line-of-sight velocities which are equal to zero. We also set all line-of-sight velocities to zero for any backscatter points on the dayside which lie below the HMB. Before fitting the spherical harmonic expansion, we also merge the line-of-sight data, using the MERGE technique (Cerisier & Senior, 1994; André et al., 1999). This resolves all measurements at a given grid point into one vector. It is worth noting that despite the padding and merging of vectors, the fitted electrostatic potentials are not forced to be zero below the HMB (due to the fitting

process using a spherical harmonic expansion) and as such, the convection cells do sometimes extend across the HMB.

### 3.1 Intermediary Maps

Examples of these average convection maps are given in Figure 1, which shows a map from the beginning of each storm phase. All other maps are included in the form of animations as supplementary material or can be downloaded as convection map files from Lancaster University’s research archive (PURE) (Walach, 2020).

From Fig. 1 we see that the convection patterns are different at the beginning of each storm phase: As expected, at the beginning of the initial phase the convection pattern is relatively small and the ionospheric convection velocities are low, whereas at the beginning of the main phase, the familiar two-cell convection pattern (e.g. Ruohoniemi & Greenwald, 1996) is enhanced and expanded, with fast return flows seen on the dusk-side. From examining these convection maps (see also supplementary material), we see that the two-cell pattern stays strong and expanded throughout the main phase. Fig. 1 and the supplementary material shows that this is further enhanced at the beginning of the recovery phase. We see from the supplementary information that the fast flows and expanded pattern stays prevalent long into the recovery phase, but start to decrease after the main phase ends.

### 3.2 Principal Component Analysis

Studying these average maps is useful to observe obvious changes in the convection, such as deviations from the two-cell convection regime, expansions and contractions, or patches of fast flows. In order to quantify changes in the convection morphologies further we now utilise principal component analysis on the data. This is a well-known technique for pattern recognition and is also known under different names, such as empirical orthogonal functions, and has been used successfully for geophysical datasets (see Baker et al., 2003; Cousins et al., 2013, 2015; Milan et al., 2015; Shore et al., 2018; Shi et al., 2020; Kim et al., 2012, and references therein). An alternative method is to use the spherical harmonics to examine changes (e.g. Grocott et al., 2012), but in this case the components are predetermined, which limits their interpretability. In PCA the components are defined by the data which allows us to find the main constituents which make

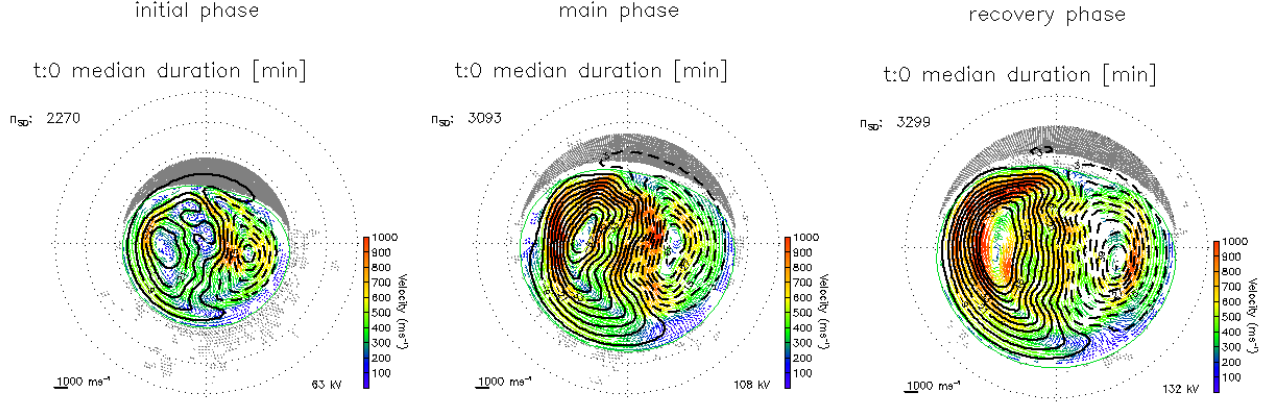


**Figure 1.** Example SuperDARN convection maps from the Superposed Epoch Analysis showing the first map of the initial (left), main (centre) and recovery phase (right), respectively. Each panel shows a map in the geomagnetic (AACGM) coordinates, whereby noon is towards the top of the page and dusk is towards the left and the grey concentric circles show equal magnetic latitudes of  $10^\circ$ , ranging from  $80^\circ$ – $40^\circ$ . The ionospheric flow vectors are colour coded by magnitude, and the electrostatic potentials are shown as equipotentials at 3 kV steps (in black). The green boundary in each panel indicates the Heppner-Maynard boundary and  $n_{SD}$  indicates the number of grid points with measurements (excluding the additional dayside padding vectors).

up the patterns. Overall, this allows us to quantify the main components to the patterns and see how they change over time.

The underlying principle is that the dataset can be decomposed into a series of basis functions which reveal underlying correlations within the data. In our case, the dataset is made of the electrostatic potential maps,  $\Phi_t$  (where  $t=0, \dots, m$ ), such that  $m = 1266$  (the median storm duration at a time resolution of 2 minutes) and each  $\Phi_t$  has  $n$ -elements, where  $n$  is given by the number of latitude by longitude grid points ( $2^\circ$  resolution). All the observations can be expressed as one  $m \times n$  matrix ( $\Phi$ ). The covariance matrix  $\Sigma$  is then given by  $\Sigma = \frac{1}{m} \Phi^T \Phi$ , where  $\Phi^T$  is the transpose of  $\Phi$ . The data  $\Phi_t$  can be expressed (or reconstructed) in terms of eigenvectors,  $\mathbf{X}_i$ , of the covariance matrix  $\Sigma$  and their components,  $\alpha_i$ , such that

$$\Phi_t = \sum_{i=1}^n \alpha_i \mathbf{X}_i. \quad (1)$$

This means components at a given time,  $\alpha_i$ , are given by

$$\alpha_i = \Phi_t \cdot \mathbf{X}_i. \quad (2)$$

Applying this method to the convection maps allows us to quantify and detect morphological changes automatically, as well as determine the primary components which make up the ionospheric electric field. In order to do this, we first scale all the ionospheric convection maps, such that they are the same size. This is necessary for the principal component analysis to work. Using different pattern sizes would involve padding areas with no data with zeros and result with no correlation between the majority of gridpoints and thus the principal component analysis method would not work. Whilst changing the size of the pattern will make the expansions and contractions invisible for the Principal Component Analysis, this information is kept, so it can be studied in conjunction with the components later. We discuss this again later in the paper and also address the expansions and contractions in WG19. We take the electrostatic potential from each map and resize the potential pattern by scaling by the Heppner-Maynard boundary (Heppner & Maynard, 1987) at midnight to  $50^\circ$  of magnetic co-latitude. We map the potential to a  $2^\circ$  latitude by  $2^\circ$  longitude grid which allows us to describe each pattern by a 1-dimensional 4500 line matrix ( $n = 4500$ ). We then calculate the mean for all storm epochs at each spatial point in the electric potential grid and subtract this from each individual map. On the remaining dataset we perform the eigen decomposition using the Householder method of eigen-decomposition (Press et al., 2007). Using only data from geomagnetic storm times for the principle component analysis means that the only bias is in our event selection, which was done using the automatic algorithm from WG19 on the Sym-H index. It is worth noting that whilst selecting by geomagnetic storm times only means we can analyse the storm-time morphologies specifically, we also impose a selection bias: although we include some quieter times during the recovery phase of the storms, this selection bias results in our mean and eigenvector patterns looking different from analyses done in previous studies (e.g. Cousins et al. (2013) used an interval which had very little geomagnetic activity and Milan (2015) used all of the available AMPERE data) and we comment on this further in the discussion section.

## 4 Results

By examining the eigenvalues, we can determine the importance of each of the eigenvectors (i.e. the component patterns that are added or subtracted together to make the convection maps). Figure 2 shows the cumulative explained variance, expressed in percentages. We see immediately that the curve converges fast: The orange dotted and dashed

lines show the  $i$ -values closest to  $>80\%$  and  $>95\%$  cut-off values, respectively. Whilst we have 4500 eigenvalues and vectors, we see from Fig. 2 that we do not need all these values to express the majority of the variability in the electric potential patterns. In fact, the variance converges fast enough that the first 6 eigenvectors explain over 80% of the variance (this is shown by the green lines). In the following parts of the manuscript we will thus focus our attention on the first 6 eigenvectors and components and examine these further.

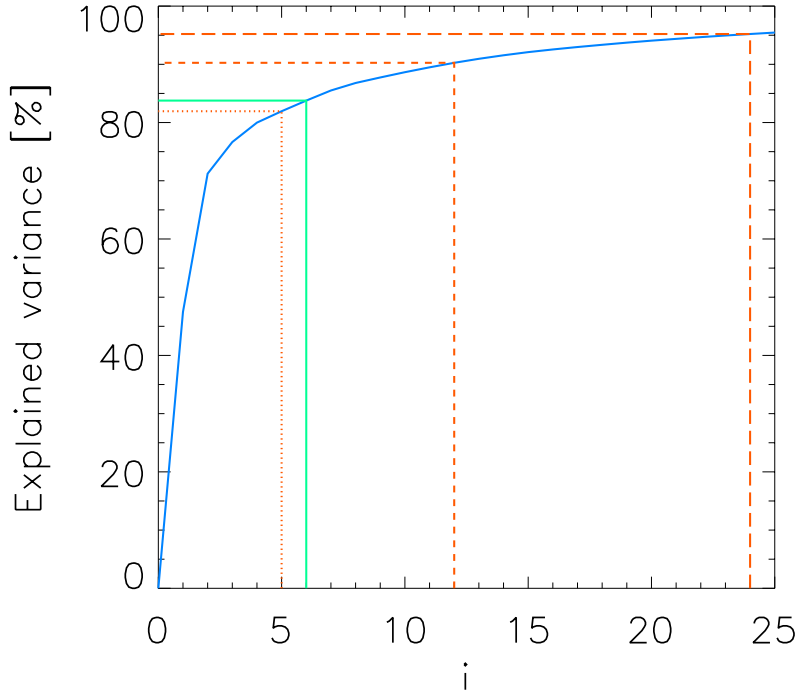


**Figure 2.** Explained variance (the first 25 eigenvalues) shown cumulatively in % of the total variance. The orange dotted, dashed and long-dashed lines show the  $i$ -values closest to 80%, 90% and 95% cut-off values, respectively, whereas the green line shows the cut-off value of the first 6 eigenvalues ( $\sim 82\%$ ).

By adding or subtracting factors of  $\mathbf{X}_i$  (where  $i=1,\dots,4500$ ) we are able to thus reconstruct the initial maps. These factors as a function of time are given by the components,  $\alpha_i$ . To simplify the interpretation of what proportion of the CPCP each component pattern holds, we have normalised each component pattern by a factor,  $f_i$ , such that terms in equation 2 become  $\mathbf{X}_i^* = \mathbf{X}_i/f_i$  and the range of each  $\mathbf{X}_i^*$  is approximately equal to one. We also scale  $\alpha_i$ , such that  $\alpha_i^* = (\alpha_i \times f_i)$ , which represents the approx-



imate CPCP each component holds and we can thus analyse this with respect to time through the storm phase. We now examine these terms ( $i = 0...6$ ) in more detail.

Figure 3 shows the primary electrostatic potential pattern components: the panel in the top left corner shows the mean pattern which was subtracted from all maps before applying the principal component analysis. The other panels show the first 6 eigenvectors (i.e. the most dominant pattern components). The pattern components  $\mathbf{X}_{1,...,6}^*$  are normalised by their CPCP, such that the colour scale approximately represent a range of 1. We will refer to this same normalisation factor,  $f_i$ , again later, as it will aid the interpretation of Figure 4. Each panel shows the eigenvector as a map in the same coordinate system as Fig. 1, whereby the magnetic pole is in the centre, noon is towards the top of the page, and dusk towards the left. The concentric dashed circles outline equal latitudes at  $10^\circ$  separation. As expected, the mean shows that a clear two-cell electric potential is dominant, with an enhancement in the dusk cell. What is less expected is that we also see an anti-clockwise rotation of the pattern about the pole. We see that  $\mathbf{X}_1^*$  is able to provide an increase or decrease in the two-cell convection potential with adding or subtracting the asymmetry from the mean pattern due to the similar rotation about the pole in the convection throat.  $\mathbf{X}_2^*$  provides morphological asymmetry by being an almost uniformly negative potential, so adding or subtracting this would strengthen one cell and weaken the other, or vice-versa.  $\mathbf{X}_1^*$  and  $\mathbf{X}_2^*$  are very similar but one can primarily strengthen or weaken the dusk cell ( $\mathbf{X}_1^*$ ) and the other the dawn cell ( $\mathbf{X}_2^*$ ).  $\mathbf{X}_{3,...,6}^*$  provide a motion towards earlier or later local times of the throat and other asymmetries, such as a variation to potential in the centre of the pattern.

The top panel of Figure 4 shows a superposed epoch analysis of the interplanetary magnetic field components,  $B_{IMF}$ , resolved into the GSM (Geocentric Solar Magnetospheric) coordinates with X in light green, Y in turquoise, and Z in dark blue. The second panel from the top shows the Heppner-Maynard boundary (in black) which the maps were scaled by, as well as the number of backscatter points per average SuperDARN map (in rose). This is followed by the median Sym-H and the CPCP (in yellow). Then we show the first six components of the eigenvectors, all as a function of storm phase-adjusted time, which are shown in grey. The black lines show the low pass filtered curve, using a 60-min centred kernel window to show the large scale changes more clearly. The first vertical dashed blue line marks the end of the initial phase and thus the beginning of the

main phase and the second dashed blue line shows the end of the main phase and the beginning of the recovery phase.

We observe that the  $B_Z$  component is clearly enhanced, especially during the main phase of the storm and that the number of backscatter points per SuperDARN map is high (this can also be seen from the animations MS01-MS03 in the Supporting Information).

The components can be of positive or negative values. The magnitude of the values indicate how much the normalised eigenvectors,  $\mathbf{X}_i^*$ , have to be amplified by and the positive or negative indicates whether or not this has to be added to or subtracted from the mean and the other components to compose the full pattern for this timestep (see also equations 1 and 2). The benefit of scaling  $\alpha_i$  by  $f_i$  (i.e. the true range of  $\mathbf{X}_i$ ), is that the scaled components  $\alpha_i^*$  approximately represent the CPCP of each pattern and thus aids interpretation.

We see immediately that much of the variability in the components is dominated by what appears to be noise, which we will investigate more quantitatively in the next section. Focusing on the black curves we see a few clear changes in  $\alpha_i^*$  with respect to the geomagnetic storm phases:  $\alpha_1^*$  shows a clear change which mirrors the HMB and Sym-H closely. At the start of the main phase, this value decreases abruptly, then stays negative and then starts to increase gradually throughout the recovery phase.  $\alpha_2^*$  also decreases as we approach end of the main phase but then increases quickly into the first part of the recovery phase, but then fluctuates about zero from about 10 normalised hours onwards but remains primarily positive. This is distinctly different to  $\alpha_1^*$  which continues to increase throughout the recovery phase.  $\alpha_3^*$  is primarily negative throughout the initial phase, then increases to a positive value through the main phase and remains primarily positive throughout the recovery phase.  $\alpha_4^*$  to  $\alpha_6^*$  remain very small and show no clear deviations from zero with respect to the storm phases.

To analyse these changes further with respect to IMF  $B_Y$  and  $B_Z$  and Sym-H, we perform a cross-correlation analysis between each of these parameters and the components. To highlight the variations over larger timescales, we use the smoothed components from Fig. 4. The best correlation coefficient,  $|r|$ , of each of these and their respective lag times,  $t$ , are given in 1. We also show  $p$  for each correlation pair, which is de-

**Table 1.**  $t$ ,  $|r|$  and  $p$  values between Sym-H;  $B_Y$ ;  $B_Z$  and each component shown in Figure 4 (black smoothed lines).

i	Sym-H:			$B_Y$ :			$B_Z$ :		
	$t$ [min]	$ r $	$p$	$t$ [min]	$ r $	$p$	$t$ [min]	$ r $	$p$
1	0	0.706	0.000	360	0.150	$4.803 \times 10^{-14}$	40	0.670	0.000
2	338	0.633	0.000	110	0.378	0.000	0	0.648	0.000
3	38	0.440	0.000	174	0.228	$1.732 \times 10^{-30}$	266	0.207	$1.755 \times 10^{-25}$
4	150	0.303	0.000	20	0.426	0.000	292	0.433	0.000
5	292	0.322	0.000	138	0.336	0.000	38	0.262	$1.287 \times 10^{-39}$
6	72	0.427	0.000	0	0.205	$6.272 \times 10^{-25}$	338	0.327	0.000

defined as the significance of the correlation. This is defined by Press et al. (2007) as

$$p = \text{erfc} \left( \frac{|r|\sqrt{N}}{\sqrt{2}} \right), \quad (3)$$

where  $\text{erfc}$  is the complementary error function and  $N$  is the number of datapoints, which is, as defined earlier,  $m$ . This value expresses the probability that in the null hypothesis of two values being uncorrelated,  $|r|$  should be larger than its observed value. A small value of  $p$  (i.e.  $p = 0$ ) thus indicates that the correlation is significant.

Table 1 shows that  $p$  is generally low, and  $p = 0$  for the cross-correlation between the first 6 components and Sym-H. This means these correlations are statistically significant. We see that the first component in particular is highly correlated with both Sym-H and  $B_Z$ , with a time lag,  $t = 0$ . This means that changes in this component are correlated with changes in Sym-H (i.e. the storm phases) and  $B_Z$  (i.e. solar wind driving). As  $i$  increases,  $|r|$  tends to decrease. The correlational pairs with  $B_Y$  are in general lower than the correlations with  $B_Z$ , which means the time variability we see in the components tend to correlate better with  $B_Z$  than  $B_Y$ . The notable exceptions here are  $\alpha_3^*$ , and  $\alpha_5^*$ , which are the only components where the correlations with  $B_Y$  are marginally higher than the correlations with  $B_Z$ .

The time lags are more difficult to interpret but indicate several patterns: The majority of the convection pattern (i.e.  $\alpha_1^*$ , which holds almost 50% of the variance) shows its best correlation at  $t = 0$ , which means this component's contribution is mostly re-

lated to Sym-H as this is how the storm phases are defined. We further note, that for any pairs where  $|r|$  is very low ( $<0.3$ ),  $t$  tends to be  $> 1$  hour, which we interpret to not be meaningful and thus do not comment further on these.

## 5 Discussion

In Fig. 4 we show that, on average, the Heppner-Maynard boundary expands to  $<50^\circ$  magnetic latitude approaching the main phase and stays expanded, well into the recovery phase when considering the lower quartile of the distribution shown in WG19. It is possible that in reality, this expansion moves to lower latitudes than  $40^\circ$  for individual storms but our observations are limited by the geographical location of the SuperDARN radars and our choice of the HMB. This expansion is coincident with the IMF  $B_Z$  component becoming more southward, leading to a higher dayside reconnection rate and thus more rapid opening of magnetic flux (Siscoe & Huang, 1985; Cowley & Lockwood, 1992; Milan et al., 2012; Walach et al., 2017). This means an expansion of the open-closed field line boundary occurs, which happens in tandem with the expansion of the convection pattern observed here (see also WG19). The high-latitude ionospheric electric field and thus convection pattern is an important mechanism for plasma transport and thus its expansion will mean the circulation of plasma at lower latitudes than was previously circulated by the high-latitude convection pattern. Zou et al. (2013) also showed that the convection pattern expanding during geomagnetic storms plays an important role in the generation and propagation of storm-enhanced densities (SEDs) seen on the dayside at mid-latitudes: Zou et al. (2013) found that there are two parts to SEDs, with the equatorward expansion of the convection pattern being the primary driver for the SED formation.

We find that the first six eigenvalues hold  $>80\%$  of the variability in the scaled ionospheric electric potential during storms (see Fig. 2). As the potential patterns which are analysed using the Principal Component Analysis are scaled by the HMB, this variability does not include the expansion or contraction of the pattern, which happens in addition to the morphological changes analysed here. The first and second eigenvectors (see  $\mathbf{X}_1^*$  and  $\mathbf{X}_2^*$  in Fig. 3) represent a dual-cell convection pattern, associated with the Dungey-cycle (e.g. Dungey, 1961, 1963; Milan, 2015; Walach et al., 2017); when  $\alpha_1^*$  and  $\alpha_2^*$  are negative  $\mathbf{X}_1^*$  and  $\mathbf{X}_2^*$  are subtracted from the mean, producing a more enhanced dual-cell convection pattern. We see from Fig. 4 that this is the case throughout the main phase

of the storm, subsiding in the recovery phase and peaking towards the end of the main phase, when solar wind driving is highest. This matches the findings of WG19, which showed that this is also when the cross polar cap potential is highest. We see from Fig. 4 that the CPCP addition from the first component changes from  $\sim 20$  kV in the initial phase to  $\sim -40$  during the main phase, which is a step change of 60 kV and slightly higher than the 40 kV step change in CPCP that was seen in WG19. This highlights that whilst this component drives a lot of the storm phase change related variability, more components need to be added to get an accurate representation of the CPCP. The second component also adds to the potential, in particular during the main phase, where its contribution reaches  $\sim 20$  kV. The first component primarily enhances or decreases the dusk-side of the potentials, whereas the second component primarily enhances or decreases the dawnside potential cell. During the main phase of the storm, when they are both negative, the convection pattern is enhanced and the two cells both increase. A few hours into the recovery phase however, when  $\alpha_1^*$  is still negative and  $\alpha_2^*$  is positive (both are at  $\sim 20$  kV magnitude), the electric potential increases on the dusk side but decreases on the dawn side, which means the dusk cell is noticeably larger than the dawn cell. We see from Fig. 4 that the following components contain slightly lower magnitudes of the potential, and decrease with each component.

The third, fourth, fifth and sixth components only add up to  $\sim 10$  kV to the convection pattern at their peak, which is minimal in the context of a CPCP between 50 to 120 kV. It is confirmed by table 1 that what looks like noise in Fig. 4 in some of the higher order components ( $\alpha_4^*$  and  $\alpha_5^*$ ), is indeed very weakly correlated with Sym-H, which means these changes are not related to the storm phases. Whilst  $\alpha_6^*$  shows a higher correlation ( $|r|=0.427$ ), it adds however less to the total CPCP and is thus less important. We see that the correlation between  $\alpha_1^*$  and Sym-H is on the other hand very high ( $|r|=0.706$ ) and significant ( $p=0.00$ ), which means this component is clearly correlated with the storm phases. This component is also highly correlated with  $B_Z$ , which is no surprise, given the high levels of solar wind driving seen during geomagnetic storms.

The third eigenvector ( $\mathbf{X}_3^*$ ) resembles the classic dual cell convection pattern but with a  $90^\circ$  rotation about the pole towards dawn. This component is therefore able to add asymmetry to the dual cell pattern in an unconventional way: its addition can move the dayside throat to earlier local times. The fourth and fifth eigenvectors ( $\mathbf{X}_4^*$  and  $\mathbf{X}_5^*$  in Fig. 3) represent asymmetric dawn-dusk changes to the patterns, which appear to mainly

rotate the convection throat on the dayside, though can rotate the nightside convection throat as well. The sixth eigenvector ( $\mathbf{X}_6^*$ ) is very symmetrical and closely resembles the second order and degree spherical harmonic pattern (e.g. see Figure 2 from Grocott et al. (2012)).

We see from Figs. 3 and 4 that the main changes with respect to storm phase which we see are primarily related to the dawn and dusk cells enhancing or decreasing. We see from Fig. 4 that the third component is primarily negative during the initial phase. Then, going into the main phase of the storm, the third component increases steadily until a change in polarity is seen in this component, right before the end of the main phase. This will not only change the cross polar cap potential, increasing it during main and recovery phases and decreasing it during the initial phase, but it will also change the location of the dayside throat. It indicates that the convection throat on the dayside reaches across the midnight-noon meridian towards dawn and becomes more noon aligned as the main phase progresses but then jumps back to be more dusk-aligned before the end of the recovery phase. For the rest of the storm time, we see this component varying slightly between positive and negative values, but primarily staying positive, meaning that the dayside throat has a tendency to be noon-aligned.

This may appear to be a result of solar wind driving and a change in the IMF  $B_Y$  component, which can move the dayside convection throat (e.g. Cowley & Lockwood, 1992; Thomas & Shepherd, 2018). This would be further evidenced as  $\alpha_4^*$  shows a mild correlation (0.426) with the IMF  $B_Y$  component, but this component adds a minor amount of electric potential and  $\alpha_3^*$  is much less correlated with  $B_Y$  (0.228) than Sym-H (0.440). We see however from the top panel in Fig. 4 that the average IMF  $B_Y$  component is near zero for these storms. In fact, 37% of the time the IMF  $B_Y$  component is positive for these storms, 38% of the time the IMF  $B_Y$  component is negative and it is zero the rest of the time. We see that it is the IMF  $B_Z$  component, which is enhanced during the main phase of the storm. That the average storm does thus not have a strong dusk-dawn component modulating the dayside flows (i.e. neither positive  $B_Y$ , nor negative  $B_Y$  are consistently dominant) is also shown in Figure 2 (panel j) in WG19, which shows that during the main phase of the storm, the IMF is overwhelmingly southward for all storms considered here. Usually when SuperDARN maps are created, base-models, which are in part parameterised by the solar wind are used (e.g. Thomas & Shepherd, 2018) such that datagaps are overcome. In this study however, no solar wind inputs were used at

all as the data coverage is very good when combining data from 7 years of geomagnetic storms. We conclude that some of this rotation in the dayside throat may be due to an IMF  $B_Y$  component, but we speculate that there are other mechanisms at play due to the inconsistency in the directionality of the  $B_Y$  component.

We theorize that some of the control in the dayside throat moving towards later local times could be due to a number of factors (or combination thereof): higher solar wind driving and the dayside reconnection rate increasing, or due to feedback through other means (e.g. thermospheric winds (Billett et al., 2018) and/or SEDs modulating the location of the throat (Zou et al., 2013, 2014) and/or the plasmaspheric plume impacting the magnetopause reconnection rate post-noon). Further evidence for the plasmaspheric plume being responsible for this moving of the dayside convection throat is available from comparing our results to those of Wharton et al. (2020): In their paper, Wharton et al. (2020) looked at the eigenfrequencies in ground magnetometer variations on the dayside during the same storm phases as ours. They found that at L-shells  $< 4$ , the eigenfrequencies in magnetometer measurements increase during the main phase of geomagnetic storms, which is due to the decrease in the plasma mass density caused by plasmaspheric erosion. This approximately corresponds to a geomagnetic latitude of  $60^\circ$  or less (see table 1 in Wharton et al. (2020)), which corresponds to the dayside throat location we see during the main phase of the storm. Wharton et al. (2020) find that at  $L > 4$  (which maps to higher latitudes and thus inside the convection pattern on the dayside), the eigenfrequencies decrease by  $\sim 50\%$  during the main phase, due to a weaker magnetic field and an enhanced plasma mass density. This may be further evidence of the plasmaspheric plume. Overall however, to find a conclusive answer for the moving of the dayside throat, further studies are needed.

Morphological changes on the nightside are more difficult to analyse and less likely to yield great insight due to the time-averaging that we have done: We know (see Table S1 in WG19) that the minimum and maximum durations of each storm phase can vary vastly (e.g. the recovery phase can be anything from  $\sim 6$  to  $\sim 163$  hours). By combining the data, such that the average convection maps match the median storm phases, we time-shift the data. Whilst the majority of storms are of similar length, it provides a good framework for studying the average storm-time responses, however other time-dependent phenomena, such as substorms are averaged out. It is well known that substorms occur frequently during geomagnetic storms and are important for the energisa-

tion of the ring current (e.g. Daglis, 2006; Sandhu et al., 2019), but Grocott et al. (2009) showed that substorms primarily produce a response in the high-latitude ionospheric convection pattern on the nightside and that ordering by onset location is important when trying to gain insight from the average convection pattern. It thus follows that although substorms commonly occur during geomagnetic storms, we do not see their signatures. We therefore cannot say if there is any substorm ordering by storm phase or time throughout the storm phases as no clear substorm signatures are seen in the average maps.

Gillies et al. (2011) studied line-of-sight SuperDARN velocity measurements during geomagnetic storms and found that an increase in IMF  $B_Z$  is accompanied by a speed increase measured with SuperDARN in the noon sector (9 to 15 MLT) and midnight sector (21 to 3 MLT) during the main phase. Gillies et al. (2011) also found a reduction in the measured plasma drift early in the main phase for intense storms, and speculated this either to be due to a reduction in the plasma drift speed or a change in the direction of the drift relative to the SuperDARN radar beam. In this study we have shown (see Fig. 4), that the addition to the convection potential increases during this time (due to the first, second and third components), which means that the convection potential increases and thus ionospheric convection velocities are likely to be also increasing. This is supported by our previous analysis (WG19) which showed that the cross polar cap potential increases during this time and thus the convection should also increase. This provides further evidence that the decrease in the plasma drifts seen by Gillies et al. (2011) during the main phase is due to the change in the direction of the flows relative to the SuperDARN radar beam (i.e. the second of their two theories).

Cousins et al. (2015) and Shi et al. (2020) used Empirical Orthogonal Function analysis to describe the modes of the Field Aligned Currents. Shi et al. (2020) split the data according to different solar wind drivers, including High Speed Streams (HSS) and transient flows related to coronal mass ejections (CMEs), both of which can be drivers of geomagnetic storms. Their patterns reflect the prevalence of the dual cell electrostatic pattern that we also see, but due to different data binning, their modes are different, making a direct comparison difficult. Overall, Shi et al. (2020) found that Sym-H is highly correlated with the modes in the transient flow category, indicating that strong geomagnetic storm activity dominates this category, which gives a strong dual cell convection pattern, as well as expansions and contractions. Both their HSS and transient categories show a mode which gives a strong asymmetry on the dayside (and would result in a sim-



ilar movement of the dayside throat that we see), which are highly correlated with Sym-H activity, but also the IMF  $B_Y$  and  $B_X$  components, and AE and solar wind temperature. Whilst the data presented by Cousins et al. (2015) did not contain any considerable geomagnetic storm activity, their results generally agree with the results from Shi et al. (2020). What does stand out when comparing results however, is that their first mode shows, similar to Shi et al. (2020), a strengthening of the pattern, which is highly correlated with AE and the IMF  $B_Z$  component. This is followed by a mode describing the expansions and contractions, which is correlated with  $B_Y$ , AE and Sym-H. The third mode from Cousins et al. (2015), describes the cusp shaping, which is also correlated with  $B_Y$ , AE and tilt, but not Sym-H. It is worth noting that Cousins et al. (2015) only showed the first few modes, and their chosen time period contains little geomagnetic activity. Cousins et al. (2013) on the other hand, used the EOF analysis to study SuperDARN data. They analysed 20 months of plasma drift data to study electric field variability and found that the first component accounted for  $\sim 50\%$  of the observed total squared electric field (which is as a proxy for the electrostatic energy per unit volume) and is primarily responsible for variations on long timescales ( $\sim 1$  hr). It is worth noting that their components look different to ours as they used a different dataset (i.e. their  $K_p$  median was 1, so they used a non-storm time dataset) for input but in general find the two-cell convection pattern to be dominant as well. Comparison between our data, Shi et al. (2020), Cousins et al. (2013) and Cousins et al. (2015) shows that using different data brings out different modes with different properties: the primary EOF in Cousins et al. (2015) strengthens the convection pattern, whereas the secondary component has a shaping function, followed by expanding and rotating modes. They further find that their top correlation for the first component is at 0.44 for the AE index, which is considerably lower than our top correlation (0.706) coefficient between Sym-H and the first component. The dayside throat in the patterns (mean and components) shown by Cousins et al. (2013) show no movement: their mean is perfectly aligned with noon, which we attribute to the fact that their input data is on average from both positive and negative  $B_Y$  with no storm effects. Conversely, the mean pattern from Milan (2015), where they applied the principal component analysis to a much larger dataset of the Birkeland currents inferred by AMPERE, showed the throat aligned with 11 and 23 MLT. This is comparable to the average conditions, also when studying SuperDARN data (e.g. Thomas & Shepherd, 2018) and indicates that the mean and the components are sensitive to the choice of input data.

As part of this study we have provided a first analysis of how the dayside throat responds to geomagnetic storms (i.e. internal magnetospheric dynamics), versus IMF  $B_Y$  conditions (i.e. external magnetospheric dynamics) and studied the timescales of day-side throat changes with respect to geomagnetic storms. In order to understand this fully, requires further study. If the dayside throat is rotated due to the plasmaspheric plume mechanism, we would expect to see the same movement in the throat (away from dusk) in the southern hemisphere, but we would expect to see it moving in the opposite sense in the southern hemisphere for any IMF  $B_Y$  related effect. We have provided a first order analysis of this and discussed potential mechanisms here but in order to find a more definitive answer, southern hemisphere data will be investigated in more detail in a future study.

## 6 Summary

We have utilised SuperDARN line-of-sight ionospheric plasma measurements to study ionospheric electric potential morphologies during geomagnetic storm time and specifically geomagnetic storm phases. We applied a principal component analysis to average ionospheric convection maps to examine the primary morphological features for the first time and using eigenvalue decomposition, we see how dominant patterns change over time (i.e. through the storm phases). The main dynamics in the morphologies that we have uncovered are happening to the ionospheric electric potential pattern on a large scale: the electric potential pattern expands and contracts; the potentials increase and decrease in strength; and the dayside convection throat rotates. We speculate that all these changes are due to the IMF  $B_Z$  component of the solar wind increasing during the main phase of the storm.

We find that

1. the first 6 eigenvectors describe over  $\sim 80\%$  of variance.
2. the two-cell convection pattern is dominant as is expected due to an expected high level of solar wind driving.
3. the first eigenvector,  $\mathbf{X}_1^*$ , provides an increase or decrease to the dusk-cell and is highly correlated with Sym-H ( $|r| = 0.706$ ).
4.  $\mathbf{X}_2^*$  provides a way to increase/decrease the dawn cell and also shows a correlation with Sym-H ( $|r| = 0.633$ ).

5.  $\mathbf{X}_3^*$  provides a motion towards earlier or later local times of the dayside convection throat.
6.  $\mathbf{X}_4^*$  to  $\mathbf{X}_6^*$  provide further ways of adding asymmetry and changes to the dual-cell convection pattern, but these are less significant ( $<20$  kV)
7. the electric potential increases through the main phase and then decreases as soon as the recovery phase is reached.
8. the dayside convection throat points towards afternoon sector before the main phase and then as the electric potential increases, the dayside throat rotates towards noon.
9. the dusk cell is generally larger than the dawn cell but during the main phase both are enhanced.

## Acknowledgments

All data used for this study are available opensource from nonprofit organizations. The authors acknowledge the use of SuperDARN data. SuperDARN is a collection of radars funded by national scientific funding agencies of Australia, Canada, China, France, Japan, South Africa, United Kingdom, and United States of America, and we thank the international PI team for providing the data. The authors acknowledge access to the SuperDARN database via the Virginia Tech SuperDARN group and their website (<http://vt.superdarn.org/>). Other data mirrors are hosted by the British Antarctic Survey (<https://www.bas.ac.uk/project/superdarn/#data>) and the University of Saskatchewan (<https://superdarn.ca/data-download>). The Radar Software Toolkit (RST) to process the SuperDARN data can be downloaded from Zenodo (<https://doi.org/10.5281/zenodo.1403226> and references). The combined data which are used to plot the maps and are used to perform the principal component analysis are available from the Lancaster University's research archive (PURE), Ionospheric Electric Field Morphologies during Geomagnetic Storm Phases 2.0, DOI:10.17635/lancaster/researchdata/344. We acknowledge the use of OMNI 1-min solar wind data, which is solar wind data that has been shifted to the location of the bow shock and can be downloaded from <https://spdf.gsfc.nasa.gov/index.htm>. M.-T. W. and A. G. were supported by Natural Environments Research Council (NERC), UK, grant nos. NE/P001556/1 and NE/T000937/1. S.E.M. was supported by the Science and Technology Facilities Council (STFC), UK, grant no. ST/S000429/1. MTW would also like to thank EGT for the helpful and insightful discussions.

## References

- Akasofu, S.-I., & Chapman, S. (1961). The ring current, geomagnetic disturbance, and the van allen radiation belts. *Journal of Geophysical Research (1896-1977)*, 66(5), 1321-1350. doi: 10.1029/JZ066i005p01321
- André, R., Villain, J.-P., Senior, C., Barthes, L., Hanuise, C., Cerisier, J.-C., & Thorolfsson, A. (1999). Toward resolving small-scale structures in ionospheric convection from superdarn. *Radio Science*, 34(5), 1165-1176. Retrieved from <https://agupubs.onlinelibrary.wiley.com/doi/abs/10.1029/1999RS900044> doi: <https://doi.org/10.1029/1999RS900044>
- Baker, J. B., Ridley, A. J., Papitashvili, V. O., & Clauer, C. R. (2003). The dependence of winter aurora on interplanetary parameters. *Journal of Geophysical Research: Space Physics*, 108(A4). Retrieved from <https://agupubs.onlinelibrary.wiley.com/doi/abs/10.1029/2002JA009352> doi: 10.1029/2002JA009352
- Billett, D. D., Grocott, A., Wild, J. A., Walach, M.-T., & Kosch, M. J. (2018). Diurnal variations in global joule heating morphology and magnitude due to neutral winds. *Journal of Geophysical Research: Space Physics*, 123(3), 2398-2411. Retrieved from <https://agupubs.onlinelibrary.wiley.com/doi/abs/10.1002/2017JA025141> doi: 10.1002/2017JA025141
- Cerisier, J.-C., & Senior, C. (1994). *Merge: A fortran program*. Cent. d'Etude des Environ. Terr. et Planet., Cent. Nat. de la Rech. Si.
- Chapman, S., & Bartels, J. (1940). *Geomagnetism, Vol. II: Analysis of the Data and Physical Theories*. Oxford University Press.
- Chapman, S., & Dyson, F. W. (1918). An outline of a theory of magnetic storms. *Proceedings of the Royal Society of London. Series A, Containing Papers of a Mathematical and Physical Character*, 95(666), 61-83. Retrieved from <https://royalsocietypublishing.org/doi/abs/10.1098/rspa.1918.0049> doi: 10.1098/rspa.1918.0049
- Chapman, S., & Ferraro, V. C. A. (1930). A new theory of magnetic storms. *Nature*, 126(3169), 129-130. doi: 10.1038/126129a0
- Chisham, G., Lester, M., Milan, S. E., Freeman, M. P., Bristow, W. a., Grocott, a., ... Walker, a. D. M. (2007). A decade of the Super Dual Auroral Radar Network (SuperDARN): Scientific achievements, new techniques and future direc-

- 662 tions. *Surveys in Geophysics*, 28(1), 33–109. doi: 10.1007/s10712-007-9017-8
- 663 Cousins, E. D. P., Matsuo, T., & Richmond, A. D. (2013). Mesoscale and large-  
 664 scale variability in high-latitude ionospheric convection: Dominant modes and  
 665 spatial/temporal coherence. *Journal of Geophysical Research: Space Physics*,  
 666 118(12), 7895–7904. Retrieved from [https://agupubs.onlinelibrary.wiley](https://agupubs.onlinelibrary.wiley.com/doi/abs/10.1002/2013JA019319)  
 667 [.com/doi/abs/10.1002/2013JA019319](https://agupubs.onlinelibrary.wiley.com/doi/abs/10.1002/2013JA019319) doi: 10.1002/2013JA019319
- 668 Cousins, E. D. P., Matsuo, T., Richmond, A. D., & Anderson, B. J. (2015). Dom-  
 669 inant modes of variability in large-scale birkeland currents. *Journal of Geo-*  
 670 *physical Research: Space Physics*, 120(8), 6722–6735. Retrieved from [https://](https://agupubs.onlinelibrary.wiley.com/doi/abs/10.1002/2014JA020462)  
 671 [agupubs.onlinelibrary.wiley.com/doi/abs/10.1002/2014JA020462](https://agupubs.onlinelibrary.wiley.com/doi/abs/10.1002/2014JA020462) doi:  
 672 10.1002/2014JA020462
- 673 Cowley, S. W. H., & Lockwood, M. (1992). Excitation and decay of solar wind-  
 674 driven flows in the magnetosphere-ionosphere system. *Annales geophys-*  
 675 *icae*, 10, 103–115. Retrieved from [http://cat.inist.fr/?aModele=](http://cat.inist.fr/?aModele=afficheN&cpsidt=5295768)  
 676 [afficheN&cpsidt=5295768](http://cat.inist.fr/?aModele=afficheN&cpsidt=5295768)
- 677 Daglis, I. A. (2006, Jun 01). Ring current dynamics. *Space Science Reviews*, 124(1),  
 678 183–202. Retrieved from <https://doi.org/10.1007/s11214-006-9104-z>  
 679 doi: 10.1007/s11214-006-9104-z
- 680 Daglis, I. A., Thorne, R. M., Baumjohann, W., & Orsini, S. (1999). The terrestrial  
 681 ring current: Origin, formation, and decay. *Reviews of Geophysics*, 37(4), 407-  
 682 438. doi: 10.1029/1999RG900009
- 683 Dungey, J. W. (1961, Jan). Interplanetary magnetic field and the auroral zones.  
 684 *Phys. Rev. Lett.*, 6, 47–48. Retrieved from [https://link.aps.org/doi/](https://link.aps.org/doi/10.1103/PhysRevLett.6.47)  
 685 [10.1103/PhysRevLett.6.47](https://link.aps.org/doi/10.1103/PhysRevLett.6.47) doi: 10.1103/PhysRevLett.6.47
- 686 Dungey, J. W. (1963). Interactions of solar plasma with the geomagnetic  
 687 field. *Planetary and Space Science*, 10, 233 - 237. Retrieved from  
 688 <http://www.sciencedirect.com/science/article/pii/0032063363900205>  
 689 doi: [https://doi.org/10.1016/0032-0633\(63\)90020-5](https://doi.org/10.1016/0032-0633(63)90020-5)
- 690 Foster, J. C. (1993). Storm time plasma transport at middle and high latitudes.  
 691 *Journal of Geophysical Research: Space Physics*, 98(A2), 1675–1689. Retrieved  
 692 from [https://agupubs.onlinelibrary.wiley.com/doi/abs/10.1029/](https://agupubs.onlinelibrary.wiley.com/doi/abs/10.1029/92JA02032)  
 693 [92JA02032](https://agupubs.onlinelibrary.wiley.com/doi/abs/10.1029/92JA02032) doi: 10.1029/92JA02032
- 694 Gabrielse, C., Pinto, V., Nishimura, Y., Lyons, L., Gallardo-Lacourt, B., & Deng, Y.

- (2019). Storm time mesoscale plasma flows in the nightside high-latitude ionosphere: A statistical survey of characteristics. *Geophysical Research Letters*, *46*(8), 4079–4088. Retrieved from <https://agupubs.onlinelibrary.wiley.com/doi/abs/10.1029/2018GL081539> doi: 10.1029/2018GL081539
- Gillies, D. M., McWilliams, K. A., St. Maurice, J.-P., & Milan, S. E. (2011). Global-scale observations of ionospheric convection during geomagnetic storms. *Journal of Geophysical Research: Space Physics*, *116*(A12). Retrieved from <https://agupubs.onlinelibrary.wiley.com/doi/abs/10.1029/2011JA017086> doi: 10.1029/2011JA017086
- Gillies, D. M., St.-Maurice, J.-P., McWilliams, K. A., & Milan, S. (2012). Global-scale observations of ionospheric convection variation in response to sudden increases in the solar wind dynamic pressure. *Journal of Geophysical Research: Space Physics*, *117*(A4). Retrieved from <https://agupubs.onlinelibrary.wiley.com/doi/abs/10.1029/2011JA017255> doi: 10.1029/2011JA017255
- Gonzalez, W. D., Joselyn, J. A., Kamide, Y., Kroehl, H. W., Rostoker, G., Tsurutani, B. T., & Vasyliunas, V. M. (1994, April). What is a geomagnetic storm? *Journal of Geophysical Research*, *99*, 5771–5792. doi: 10.1029/93JA02867
- Graham, G. (1724). Iv. an account of observations made of the variation of the horizontal needle at london, in the latter part of the year 1772, and beginning of 1723. *Philosophical Transactions of the Royal Society of London*, *33*(383), 96–107. doi: 10.1098/rstl.1724.0020
- Greenwald, R. A., Baker, K. B., Dudeney, J. R., Pinnock, M., Jones, T. B., Thomas, E. C., ... Yamagishi, H. (1995). Darn/superdarn. *Space Science Reviews*, *71*(1), 761–796. doi: 10.1007/BF00751350
- Grocott, A., Milan, S. E., Imber, S. M., Lester, M., & Yeoman, T. K. (2012). A quantitative deconstruction of the morphology of high-latitude ionospheric convection. *Journal of Geophysical Research: Space Physics*, *117*(A5). Retrieved from <https://agupubs.onlinelibrary.wiley.com/doi/abs/10.1029/2012JA017580> doi: 10.1029/2012JA017580
- Grocott, A., Wild, J. A., Milan, S. E., & Yeoman, T. K. (2009). Superposed epoch analysis of the ionospheric convection evolution during substorms: onset latitude dependence. *Annales Geophysicae*, *27*(2), 591–

600. Retrieved from <https://www.ann-geophys.net/27/591/2009/> doi:  
10.5194/angeo-27-591-2009
- Hairston, M. R., & Heelis, R. A. (1993). *High-latitude electric field studies using dmsp data* (Tech. Rep.). Texas University at Dallas Richardson Center for Space Sciences.
- Heppner, J. P., & Maynard, N. C. (1987). Empirical high-latitude electric field models. *Journal of Geophysical Research*, 92(A5), 4467–4489. doi: 10.1029/JA092iA05p04467
- Huba, J. D., Joyce, G., Sazykin, S., Wolf, R., & Spiro, R. (2005). Simulation study of penetration electric field effects on the low- to mid-latitude ionosphere. *Geophysical Research Letters*, 32(23). Retrieved from <https://agupubs.onlinelibrary.wiley.com/doi/abs/10.1029/2005GL024162> doi: 10.1029/2005GL024162
- Hutchinson, J. A., Wright, D. M., & Milan, S. E. (2011). Geomagnetic storms over the last solar cycle: A superposed epoch analysis. *Journal of Geophysical Research: Space Physics*, 116(9), 1–16. doi: 10.1029/2011JA016463
- Imber, S. M., Milan, S. E., & Lester, M. (2013). The heppner-maynard boundary measured by superdarn as a proxy for the latitude of the auroral oval. *Journal of Geophysical Research: Space Physics*, 118(2), 685–697. doi: 10.1029/2012JA018222
- Iyemori, T. (1990). Storm-time magnetospheric currents inferred from mid-latitude geomagnetic field variations. *Journal of geomagnetism and geoelectricity*, 42(11), 1249–1265. doi: 10.5636/jgg.42.1249
- Jolliffe, I. T. (2002). *Principle component analysis*. Springer.
- Kamide, Y., Richmond, A. D., & Matsushita, S. (1981). Estimation of ionospheric electric fields, ionospheric currents, and field-aligned currents from ground magnetic records. *Journal of Geophysical Research: Space Physics*, 86(A2), 801–813. Retrieved from <https://agupubs.onlinelibrary.wiley.com/doi/abs/10.1029/JA086iA02p00801> doi: 10.1029/JA086iA02p00801
- Kane, T. A., & Makarevich, R. A. (2010). Hf radar observations of the f region ionospheric plasma response to storm sudden commencements. *Journal of Geophysical Research: Space Physics*, 115(A7). Retrieved from <https://agupubs.onlinelibrary.wiley.com/doi/abs/10.1029/2009JA014974> doi: 10.1029/

- 2009JA014974
- Kikuchi, T., Hashimoto, K. K., & Nozaki, K. (2008). Penetration of magnetospheric electric fields to the equator during a geomagnetic storm. *Journal of Geophysical Research: Space Physics*, 113(A6). Retrieved from <https://agupubs.onlinelibrary.wiley.com/doi/abs/10.1029/2007JA012628> doi: 10.1029/2007JA012628
- Kim, H.-J., Lyons, L. R., Ruohoniemi, J. M., Frissell, N. A., & Baker, J. B. (2012). Principal component analysis of polar cap convection. *Geophysical Research Letters*, 39(11). Retrieved from <https://agupubs.onlinelibrary.wiley.com/doi/abs/10.1029/2012GL052083> doi: 10.1029/2012GL052083
- Lin, C. H., Richmond, A. D., Heelis, R. A., Bailey, G. J., Lu, G., Liu, J. Y., ... Su, S.-Y. (2005). Theoretical study of the low- and midlatitude ionospheric electron density enhancement during the october 2003 superstorm: Relative importance of the neutral wind and the electric field. *Journal of Geophysical Research: Space Physics*, 110(A12). Retrieved from <https://agupubs.onlinelibrary.wiley.com/doi/abs/10.1029/2005JA011304> doi: 10.1029/2005JA011304
- Loewe, C. A., & Prölss, G. W. (1997). Classification and mean behavior of magnetic storms. *Journal of Geophysical Research: Space Physics*, 102(A7), 14209-14213. doi: 10.1029/96JA04020
- Mannucci, A. J., Tsurutani, B. T., Abdu, M. A., Gonzalez, W. D., Komjathy, A., Echer, E., ... Anderson, D. (2008). Superposed epoch analysis of the day-side ionospheric response to four intense geomagnetic storms. *Journal of Geophysical Research: Space Physics*, 113(A3). Retrieved from <https://agupubs.onlinelibrary.wiley.com/doi/abs/10.1029/2007JA012732> doi: 10.1029/2007JA012732
- Milan, S. E. (2015). Sun et lumière: solar wind-magnetosphere coupling as deduced from ionospheric flows and polar auroras. In D. Southwood, S. W. H. Cowley FRS, & S. Mitton (Eds.), *Magnetospheric plasma physics: The impact of jim dungeys research* (pp. 1-271). Astrophysics and Space Science Proceedings 41, Springer. doi: 10.1007/978-3-319-18359-6\_2
- Milan, S. E., Carter, J. A., Korth, H., & Anderson, B. J. (2015). Principal component analysis of birkeland currents determined by the active magnetosphere



- and planetary electrodynamics response experiment. *Journal of Geophysical Research: Space Physics*, 120(12), 10,415–10,424. Retrieved from <https://agupubs.onlinelibrary.wiley.com/doi/abs/10.1002/2015JA021680> doi: 10.1002/2015JA021680
- Milan, S. E., Clausen, L. B. N., Coxon, J. C., Carter, J. A., Walach, M.-T., Laundal, K., ... Anderson, B. J. (2017). Overview of solar wind–magnetosphere–ionosphere–atmosphere coupling and the generation of magnetospheric currents. *Space Science Reviews*, 206(1), 547–573. Retrieved from <https://doi.org/10.1007/s11214-017-0333-0> doi: 10.1007/s11214-017-0333-0
- Milan, S. E., Gosling, J. S., & Hubert, B. (2012, mar). Relationship between interplanetary parameters and the magnetopause reconnection rate quantified from observations of the expanding polar cap. *Journal of Geophysical Research*, 117(A3), A03226. doi: 10.1029/2011JA017082
- Nishitani, N., Ruohoniemi, J. M., Lester, M., Baker, J. B. H., Koustov, A. V., Shepherd, S. G., ... Kikuchi, T. (2019). Review of the accomplishments of mid-latitude super dual auroral radar network (superdarn) hf radars. *Progress in Earth and Planetary Science*, 6(1), 27. doi: 10.1186/s40645-019-0270-5
- Press, W. H., Teukolsky, S. A., T., V. W., & P., F. B. (2007). *Numerical recipes: The art of scientific computing*. Cambridge University Press.
- Ruohoniemi, J. M., & Baker, K. B. (1998). Large-scale imaging of high-latitude convection with Super Dual Auroral Radar Network HF radar observations. *Journal of Geophysical Research*, 103(A9), 20797. doi: 10.1029/98JA01288
- Ruohoniemi, J. M., & Greenwald, R. A. (1996). Statistical patterns of high-latitude convection obtained from Goose Bay HF radar observations. *Journal of Geophysical Research*, 101(A10), 21743. Retrieved from <http://doi.wiley.com/10.1029/96JA01584> doi: 10.1029/96JA01584
- Sandhu, J. K., Rae, I. J., Freeman, M. P., Gkioulidou, M., Forsyth, C., Reeves, G. D., ... Walach, M.-T. (2019). Substorm-ring current coupling: A comparison of isolated and compound substorms. *Journal of Geophysical Research: Space Physics*, 124(8), 6776–6791. Retrieved from <https://agupubs.onlinelibrary.wiley.com/doi/abs/10.1029/2019JA026766> doi: 10.1029/2019JA026766
- Shepherd, S. G., & Ruohoniemi, J. M. (2000). Electrostatic potential patterns in

- the high-latitude ionosphere constrained by superdarn measurements. *Journal of Geophysical Research: Space Physics*, 105(A10), 23005-23014. Retrieved from <https://agupubs.onlinelibrary.wiley.com/doi/abs/10.1029/2000JA000171> doi: 10.1029/2000JA000171
- Shi, Y., Knipp, D. J., Matsuo, T., Kilcommons, L., & Anderson, B. (2020). Modes of (facs) variability and their hemispheric asymmetry revealed by inverse and assimilative analysis of iridium magnetometer data. *Journal of Geophysical Research: Space Physics*, 125(2), e2019JA027265. Retrieved from <https://agupubs.onlinelibrary.wiley.com/doi/abs/10.1029/2019JA027265> (e2019JA027265 2019JA027265) doi: 10.1029/2019JA027265
- Shore, R. M., Freeman, M. P., & Gjerloev, J. W. (2018). An empirical orthogonal function reanalysis of the northern polar external and induced magnetic field during solar cycle 23. *Journal of Geophysical Research: Space Physics*, 123(1), 781-795. Retrieved from <https://agupubs.onlinelibrary.wiley.com/doi/abs/10.1002/2017JA024420> doi: 10.1002/2017JA024420
- Singer, S. F. (1957). A new model of magnetic storms and aurorae. *Eos, Transactions American Geophysical Union*, 38(2), 175-190. doi: 10.1029/TR038i002p00175
- Siscoe, G. L., & Huang, T. S. (1985). Polar cap inflation and deflation. *Journal of Geophysical Research*, 90(A1), 543-547.
- Sugiura, M. (1964). Hourly values of equatorial dst for the igy. *Ann. Int. Geophys. Yr.*, 35, 9.
- SuperDARN Data Analysis Working Group, P. m., Thomas, E. G., Ponomarenko, P. V., Billett, D. D., Bland, E. C., Burrell, A. G., ... Walach, M.-T. (2018, August). *Superdarn radar software toolkit (rst) 4.2*. Retrieved from <https://doi.org/10.5281/zenodo.1403226> doi: 10.5281/zenodo.1403226
- Thomas, E. G., Baker, J. B. H., Ruohoniemi, J. M., Clausen, L. B. N., Coster, A. J., Foster, J. C., & Erickson, P. J. (2013). Direct observations of the role of convection electric field in the formation of a polar tongue of ionization from storm enhanced density. *Journal of Geophysical Research: Space Physics*, 118(3), 1180-1189. Retrieved from <https://agupubs.onlinelibrary.wiley.com/doi/abs/10.1002/jgra.50116> doi: 10.1002/jgra.50116
- Thomas, E. G., & Shepherd, S. G. (2018, apr). Statistical Patterns of Ionospheric

- Convection Derived From Mid-latitude, High-Latitude, and Polar Super-DARN HF Radar Observations. *Journal of Geophysical Research: Space Physics*, 123(4), 3196–3216. Retrieved from <http://doi.wiley.com/10.1002/2018JA025280> doi: 10.1002/2018JA025280
- Walach, M.-T. (2020). *Ionospheric electric field morphologies during geomagnetic storm phases 2.0*. Lancaster University PURE. Retrieved from [http://www.research.lancs.ac.uk/portal/en/datasets/ionospheric-electric-field-morphologies-during-geomagnetic-storm-phases-20\(744a0943-d67d-4380-bfaf-f919df71c8ef\).html](http://www.research.lancs.ac.uk/portal/en/datasets/ionospheric-electric-field-morphologies-during-geomagnetic-storm-phases-20(744a0943-d67d-4380-bfaf-f919df71c8ef).html) doi: 10.17635/lancaster/researchdata/344
- Walach, M.-T., & Grocott, A. (2019). Superdarn observations during geomagnetic storms, geomagnetically active times, and enhanced solar wind driving. *Journal of Geophysical Research: Space Physics*, 124(7), 5828–5847. Retrieved from <https://agupubs.onlinelibrary.wiley.com/doi/abs/10.1029/2019JA026816> doi: 10.1029/2019JA026816
- Walach, M.-T., Milan, S. E., Yeoman, T. K., Hubert, B. A., & Hairston, M. R. (2017). Testing nowcasts of the ionospheric convection from the expanding and contracting polar cap model. *Space Weather*, 15(4), 623–636. doi: 10.1002/2017SW001615
- Wharton, S. J., Rae, I. J., Sandhu, J. K., Walach, M.-T., Wright, D. M., & Yeoman, T. K. (2020). The changing eigenfrequency continuum during geomagnetic storms: Implications for plasma mass dynamics and ulf wave coupling. *Journal of Geophysical Research: Space Physics*, n/a(n/a), e2019JA027648. Retrieved from <https://agupubs.onlinelibrary.wiley.com/doi/abs/10.1029/2019JA027648> (e2019JA027648 2019JA027648) doi: 10.1029/2019JA027648
- Wilson, G. R., Burke, W. J., Maynard, N. C., Huang, C. Y., & Singer, H. J. (2001). Global electrodynamics observed during the initial and main phases of the july 1991 magnetic storm. *Journal of Geophysical Research: Space Physics*, 106(A11), 24517–24539. doi: 10.1029/2000JA000348
- Zou, S., Moldwin, M. B., Ridley, A. J., Nicolls, M. J., Coster, A. J., Thomas, E. G., & Ruohoniemi, J. M. (2014). On the generation/decay of the storm-enhanced density plumes: Role of the convection flow and field-aligned ion flow. *Journal of Geophysical Research: Space Physics*, 119(10), 8543–8559. Retrieved

893 from <https://agupubs.onlinelibrary.wiley.com/doi/abs/10.1002/>  
894 2014JA020408 doi: 10.1002/2014JA020408  
895 Zou, S., Ridley, A. J., Moldwin, M. B., Nicolls, M. J., Coster, A. J., Thomas, E. G.,  
896 & Ruohoniemi, J. M. (2013). Multi-instrument observations of sed during  
897 2425 october 2011 storm: Implications for sed formation processes. *Jour-*  
898 *nal of Geophysical Research: Space Physics*, 118(12), 7798-7809. Retrieved  
899 from <https://agupubs.onlinelibrary.wiley.com/doi/abs/10.1002/>  
900 2013JA018860 doi: 10.1002/2013JA018860

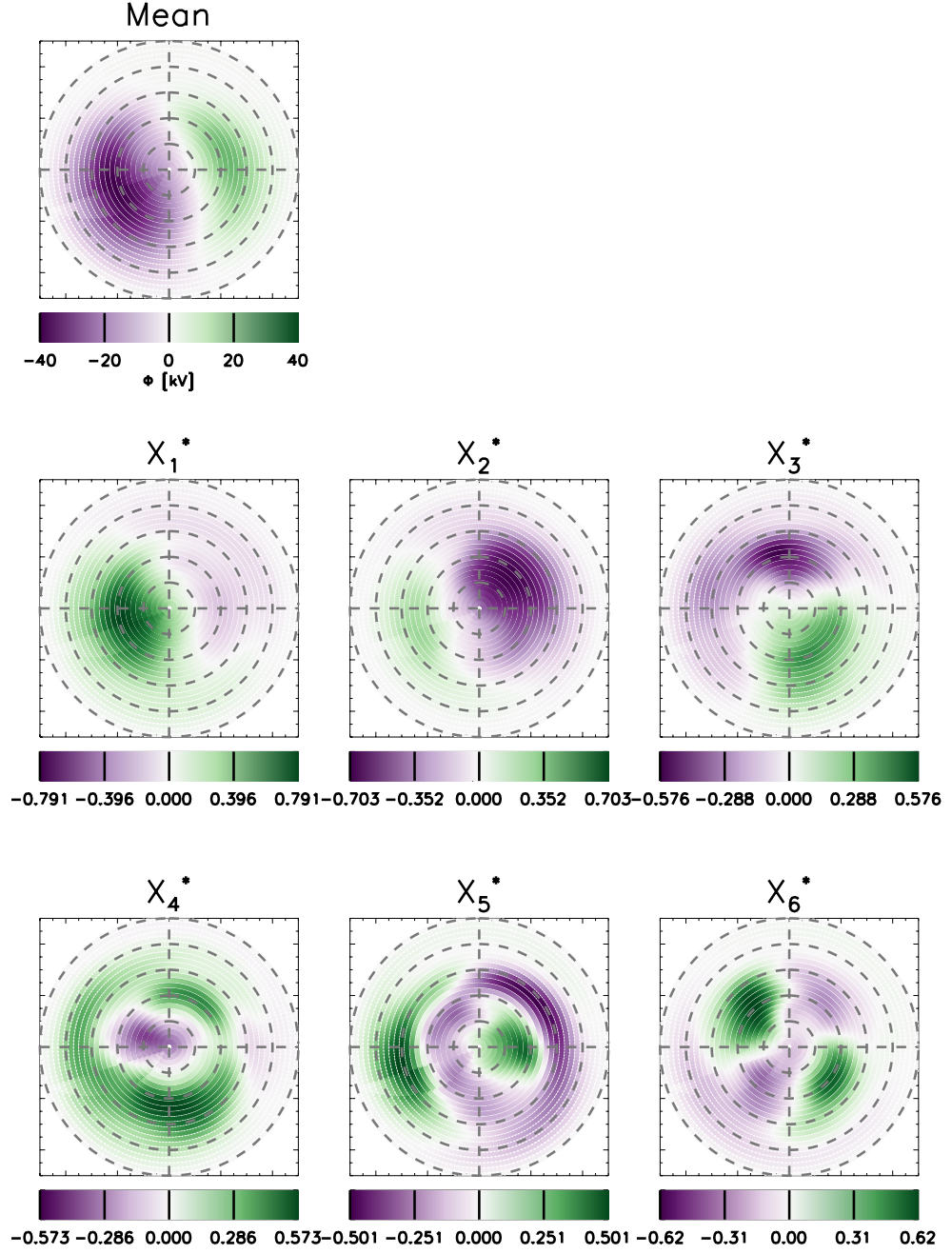


**Figure 3.** Ionospheric electric field component patterns showing the mean for geomagnetic storms (top left), followed by the patterns corresponding to the first 6 eigenvectors of the Principal Component Analysis. Each pattern is centred on the geomagnetic pole, with 12:00 magnetic local time pointing towards the top of the page, and dusk towards the left. Lines of geomagnetic latitudes are indicated from  $40^\circ$  to  $90^\circ$  by the dashed grey circles.

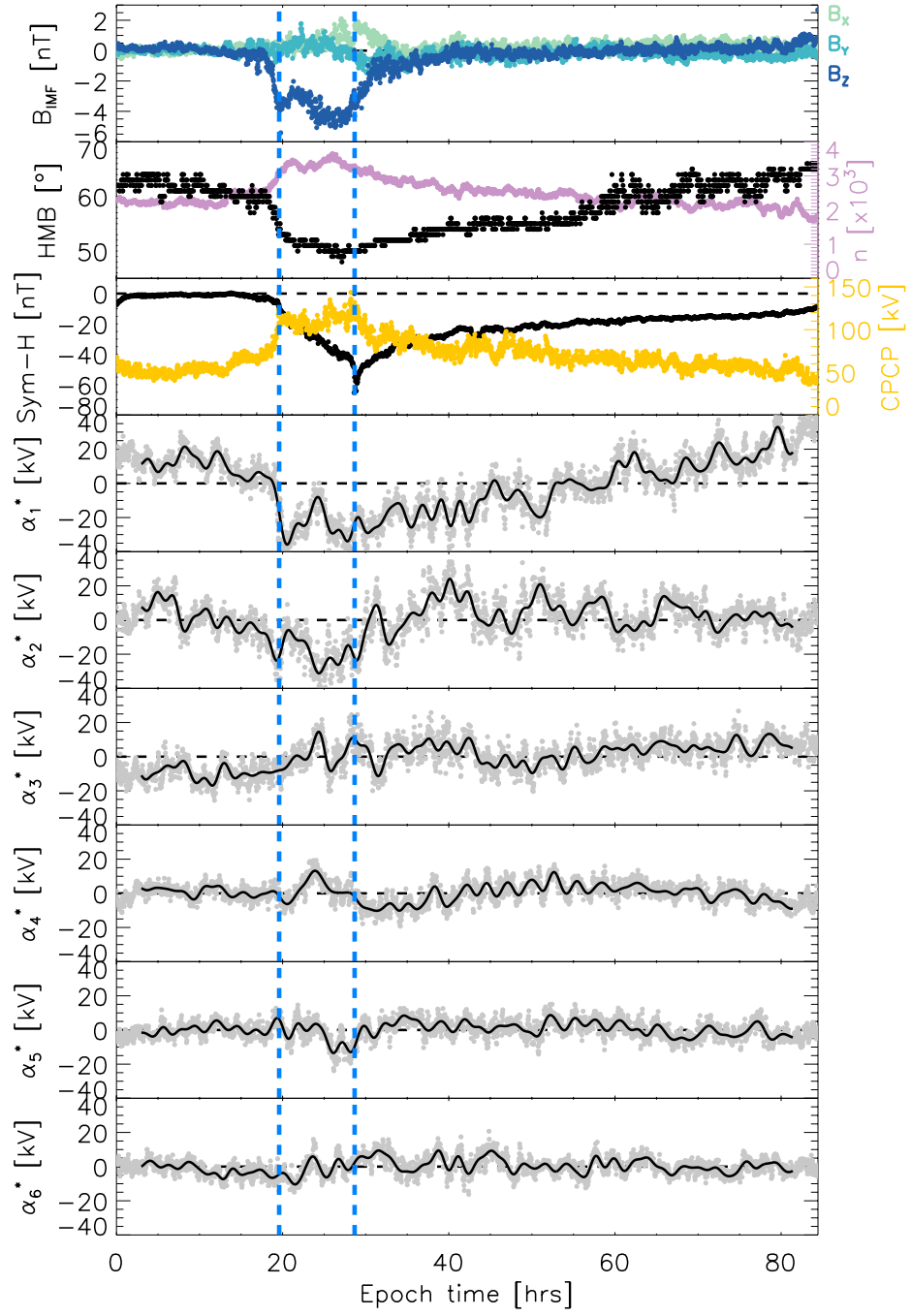


**Figure 4.** Panels showing the average (median) interplanetary magnetic field,  $B_{IMF}$  (top panel), where the light green is  $B_X$ , turquoise is  $B_Y$  and the dark blue is  $B_Z$ ; the Heppner Maynard Boundary and the number of backscatter points per average SuperDARN map (in rose) (second panel from the top); followed by the median Sym-H index and the CPCP (yellow). The panels showing  $\alpha_1^*$  to  $\alpha_6^*$  show the first 6 normalised components of the Principal Component Analysis with respect to time through the storm phases. The components are shown in grey and the black lines shows them with a 60-minute low pass filter applied. The boundaries between the initial and main, and the main and recovery phases are shown by the dashed blue vertical lines.

# Supporting Information for ”Average Ionospheric Electric Field Morphologies during Geomagnetic Storm Phases”

M.-T. Walach<sup>1</sup>, A. Grocott<sup>1</sup>, S.E. Milan<sup>2</sup>

<sup>1</sup>Lancaster University, Lancaster, LA1 4YW, UK

<sup>2</sup>University of Leicester, Leicester, LE1 7RH, UK

## Contents of this file

1. Captions for Movies S1 to S3

## Additional Supporting Information (Files uploaded separately)

1. Movies S1 to S3

**Introduction** The data accompanying the main manuscript are three animations in gif format, which contain the individual SuperDARN convection map files used for the principal component analysis for the main analysis. Each animation contains the convection maps for one of the storm phases: initial, main and recovery phase. The maps are time-normalized superposed epoch analyses, such that the duration of each phase matches the median duration of each phase (this is explained in the main manuscript), using a 2-minute cadence. The maps were created using the Radar Software Toolkit version 4.2

---

Corresponding author: M.-T. Walach, Lancaster University, Lancaster, LA1 4YW, UK  
([m.walach@lancaster.ac.uk](mailto:m.walach@lancaster.ac.uk))

January 12, 2021, 2:07pm

(SuperDARN Data Analysis Working Group et al., 2018) (see main manuscript for more detail). Each map shows the gridded and fitted radar data with respect to the geomagnetic pole, where noon is towards the top, midnight towards the bottom, dusk towards the left and dawn towards the right. The dotted circles show lines of equal geomagnetic latitude, which are  $10^\circ$  apart. The thick black (dashed and non-dashed) lines show the electrostatic potential contours, which were obtained by performing a spherical harmonic analysis of the 8th order (Ruohoniemi & Greenwald, 1996). All line of sight data has been merged before the fitting was applied and zero velocity vectors were artificially added on the dayside below the HMB.

**Movie S1.** Animation of the convection maps for the initial phase. **Movie S2.** Animation of the convection maps for the main phase. **Movie S3.** Animation of the convection maps for the recovery phase.

## References

- Ruohoniemi, J. M., & Greenwald, R. A. (1996). Statistical patterns of high-latitude convection obtained from Goose Bay HF radar observations. *Journal of Geophysical Research*, 101(A10), 21743. Retrieved from <http://doi.wiley.com/10.1029/96JA01584> doi: 10.1029/96JA01584
- SuperDARN Data Analysis Working Group, P. m., Thomas, E. G., Ponomarenko, P. V., Billett, D. D., Bland, E. C., Burrell, A. G., ... Walach, M.-T. (2018, August). *Superdarn radar software toolkit (rst) 4.2*. Retrieved from <https://doi.org/10.5281/zenodo.1403226> doi: 10.5281/zenodo.1403226